7. ASSESSMENT OF REVERSED-SHEAR POWER PLANTS

Charles G. Bathke
Stephen C. Jardin
David A. Ehst
Charles Kessel, Jr.
Tak-Kuen Mau
Farrokh Najmabadi

Contents

7.1. INTRODUCTION 7-1

7.2. PHYSICS BASIS 7-2

7.2.1. MHD Stability and Bootstrap Current 7-2

7.2.2. Current Drive 7-8

7.3. SYSTEMS ASSESSMENT 7-11

7.3.1. Plasma Minor Radius 7-13

7.3.2. Plasma Ion Temperature 7-14

7.3.3. Plasma Aspect Ratio 7-16

7.3.4. Design Point Determination 7-18

7.4. SUMMARY AND CONCLUSIONS 7-23

REFERENCES 7-24

7. ASSESSMENT OF REVERSED-SHEAR POWER PLANTS

7.1. INTRODUCTION

The reversed-shear plasma configuration has considerable potential for providing the basis of an attractive fusion power plant. The benefits of this configuration are that it achieves both high β_N and high β, it obtains large bootstrap current fractions with very good current profile alignment, and it appears to provide the transport suppression necessary to sustain the pressure profile that is consistent with the higher β and high bootstrap current [1–3]. The primary characteristics of a reversed shear plasma are a hollow current profile, a non-monotonic safety-factor (q) profile, and relatively peaked pressure profiles. The hollow current-density profile gives rise to a safety-factor profile, which initially decreases from its value at the plasma center to a minimum value, and then rises to its value at the plasma edge. The name "reversed shear" arises from the fact that the safety-factor in a conventional tokamak plasma rises monotonically from the plasma center to the edge. It is the initial decrease in the q-value away from the magnetic axis that provides negative magnetic shear, which is responsible for stability to $n \rightarrow \infty$ ballooning modes and suppression of plasma transport.

Recent experiments [4–6] have demonstrated transiently the improved MHD stability and suppression of plasma particle and energy transport. Complete demonstration of all the favorable properties simultaneously will require steady-state conditions, which are not accessible in present experimental devices.

In this section, we present our assessment of tokamak power plants operating with a reversed-shear plasma. This assessment includes the results of detailed physics calculations and parametric systems analyses. The assessment of engineering options of Sec. 6 applies to this regime of operation (noting that reversed-shear plasmas probably lead to devices with higher neutron and surface heat loads). Overall the reversed-shear plasma offers the best economic performance of physics options examined and the data base for this regime, while small, is growing rapidly.

7.2. PHYSICS BASIS

7.2.1. MHD Stability and Bootstrap Current

Several reversed-shear equilibria were examined in order to assess the balance between maximizing β (fusion power density) and minimizing the current-drive (recirculating) power. The plasma equilibria are determined using a fixed boundary flux coordinate equilibrium calculation. Ideal MHD stability calculations are done for $n \rightarrow \infty$ ballooning modes and $n = 1-4$ external kink modes, with a conducting wall placed at 0.3 times the minor radius, a, measured from the plasma boundary. All configurations reported here operate at 90% of the maximum stable β in order to provide an acceptable margin to the stability boundary. The analysis was performed at four aspect ratios: 3.0, 3.5, 4.0, and 4.5, and the results are presented in Table 7.2-I. These results provide the basis for further physics analysis as well the systems modeling to determine the optimum aspect ratio and strawman configuration.

The bootstrap current is calculated using the full Hirshman-Sigmar expression with a velocity space representation of the viscosity coefficients [7]. The pressure gradient profile is the dominant factor in setting the bootstrap current-density profile. This is an important consideration when searching for MHD stable equilibria. The bootstrap-current profile is naturally hollow, which provides for very good profile alignment with the reversed-shear current profile required for MHD stability.

The plasma particle and energy transport are not explicitly modeled. Plasma temperature and density profiles are only made to roughly agree with experimental observations for reversed shear configurations. Once a stable plasma equilibrium is found, the plasma temperature is adjusted to provide the largest and best aligned bootstrap current profile. Since a transport barrier exists in the region of the minimum safety factor, efforts are made to restrict the dominant gradients of the temperature and density in this vicinity.

The pressure profile (p) has a very strong impact on both the MHD stability and the bootstrap-current alignment. In our analysis, the following form for the pressure profile is used:

$$p \;=\; p_0(1-\hat{\psi}^{\alpha})^2 \,. \qquad (7.2\text{-}1)$$

where p_0 is the central pressure and $\hat{\psi}$ is the normalized poloidal flux. The exponent α is varied from 1.0 to 1.8 for the purpose of examining the impact of profile broadness. For the more peaked pressure profiles, the low-n kink modes become the limiting instability, in

Table 7.2-I.
Several Reversed-Shear Plasma Configurations[(a)]

	$A = 3.0$	$A = 3.5$	$A = 4.0$	$A = 4.5$
Plasma current (MA)	16.3	13.4	11.4	10.0
On-axis toroidal field (T)	6.01	6.75	7.50	8.31
Major radius (m)	5.40	5.40	5.40	5.40
Minor radius (m)	1.80	1.54	1.35	1.21
Elongation, κ_{95}	1.80	1.80	1.80	1.80
Triangularity, δ_{95}	0.50	0.50	0.50	0.50
Density profile peaking factor, $n_o/\langle n\rangle$	1.52	1.48	1.55	1.72
Temperature profile peaking factor, $T_o/\langle T\rangle$	1.60	1.66	1.68	1.49
Pressure profile peaking factor, $p_o/\langle p\rangle$	2.07	2.09	2.13	2.21
Location of kink-stabilization wall[(b)]	$0.3a$	$0.3a$	$0.3a$	$0.3a$
Poloidal β	1.75	1.95	2.05	2.16
Toroidal β	7.48%	6.14%	4.91%	4.02%
Toroidal β^*	9.17%	7.55%	6.08%	5.05%
Normalized β_N	4.97%	4.76%	4.36%	4.05%
Maximum β_N	5.50%	5.30%	4.85%	4.50%
Bootstrap current (MA)	14.1	11.7	9.85	9.02
Driven current, I_{CD} (MA)	1.80	1.50	1.40	0.95
On-axis safety factor, q_o	2.88	2.88	2.70	2.50
Minimum safety factor, q_{min}	2.62	2.51	2.39	2.18
Location of q_{min}, $\hat{\psi}(q_{min})$	0.66	0.68	0.68	0.58
Edge safety factor, q_e	3.88	3.61	3.47	3.46
Edge safety factor, q_*	2.35	2.35	2.35	2.35
Internal inductance, $l_i(3)$	0.39	0.41	0.43	0.48

(a) All equilibria operate at 90% of maximum theoretical β.

(b) Distance from the plasma edge normalized to minor radius.

particular, the $n = 3$ mode (with the conducting shell at $0.3a$). These cases with peaked pressure profiles have the highest β limit. However, in these equilibria the bootstrap current-density profile peaks near the plasma center, where a hollow current profile is needed. Thus, the highest β equilibria have poor bootstrap alignment.

As the pressure profile is broadened, it was found that the maximum β decreased. However, this also leads to the bootstrap current peaking further from the plasma center resulting in improved current profile alignment. When the position of the minimum in the safety factor is fixed at its maximum distance from the plasma center, as the plasma pressure profile is broadened, the $n \to \infty$ ballooning modes become the limiting instability.

The broadest pressure profiles produce the best bootstrap-current alignment with the desired current profile. These cases, however, have a low β limit and bootstrap fractions approaching unity cannot be attained. A tradeoff between the β limit and bootstrap alignment led to the pressure profile exponent, $\alpha = 1.4$ for all aspect ratios. This causes the $n \to \infty$ ballooning and low-n kink stability limits to nearly coincide, while providing excellent bootstrap-current alignment. The value of the pressure exponent is fixed for all subsequent calculations, unless otherwise stated.

The plasma parallel current-density profile is assumed to have the form:

$$\frac{\langle j \cdot B \rangle}{\langle B \cdot \nabla \phi \rangle} \quad = \quad j_0(1-\hat{\psi}) + j_1 \frac{d^2(1-\hat{\psi})^2\hat{\psi}}{(\hat{\psi}-\psi_o)+d^2}\,, \tag{7.2-2}$$

The adjustable parameters j_0, j_1, and d are chosen so as to place the minimum in the safety factor as far out as possible while keeping the edge q between 3.5 and 4.0. This moves the low-n kink mode structure closer to the stabilizing conducting wall which is placed at a distance of $0.3a$ from the plasma boundary. In addition, the central safety factor is chosen to provide a sufficient degree of negative magnetic shear, approximately given by $q_o - q_{min} \geq 0.3$. For all cases, q_{min} is kept above 2.0, and q_o is kept below 3.0 to avoid multiple integral safety-factor values, which serves as an approximate guideline for avoiding resistive instabilities. The corresponding current profiles give rise to minimum-q locations in the range of $0.6 \leq \hat{\psi} \leq 0.7$, while the q_{min} values vary from 2.2 to 2.6.

Scans of equilibria with different aspect ratios showed that decreasing aspect ratio results in an increase in β_N. Since for a fixed q_*, the plasma current also increases with a decreasing aspect ratio, the plasma β will be higher for lower aspect ratio equilibria. On the other hand, while in all cases the plasma driven current (bootstrap, diamagnetic, and Pfirsch-Schluter) exceeds 89%, the off-axis current-drive power increases with decreasing

aspect ratio. Therefore, decreasing aspect ratios results in a higher β and a higher current-drive power. In order to find the optimum aspect ratio, the results listed Table 7.2-I together with detailed current-drive calculations (Sec. 7.2.2) were used in the systems code analysis (Sec. 7.3).

7.2.1.1. Conducting shell for low-n kink modes

A conducting wall is required for these configurations to obtain the high β values. Since no second stability regime has been found for the low-n kink modes, as there is for the $n \to \infty$ ballooning modes [8, 9], it is necessary to utilize a conducting wall to access high pressures where a fusion power plant can become significantly more attractive. Recent experiments [10] and theory [11] indicate that a resistive wall can stabilize the low-n kink modes if the plasma is rotating and a dissipation mechanism in the plasma is present.

The reversed-shear configuration can better utilize a wall than a plasma with a monotonic safety-factor profile. This arises because of the presence of the zero magnetic shear ($dq/d\psi = 0$) region which causes the kink mode structure to shift to that vicinity. If the zero shear region is moved closer to the plasma edge, one moves the plasma displacements associated with the instability closer to the conducting wall, thereby making the wall more effective at suppressing them. In the absence of a conducting wall, the reversed-shear plasmas typically obtain similar or lower β values as compared to plasmas with monotonic safety-factor profiles.

From theoretical analysis one can approximate the requirements to stabilize the low-n kink modes. The plasma must rotate at about 5%–10% of the Alfven speed, resulting in a 2.8 to 5.6×10^5 m/s rotation speed. The actual conducting wall should be located at the ideal wall position for the plasma mode to provide the greatest margin to the resistive wall mode, which occurs when the wall is too close to the plasma. Therefore, in our analysis the conducting wall is located at $0.3a$ measured from the plasma boundary. The wall has conductivity and thickness requirements that are given by $\Delta/\eta > 1.5 \times 10^4$, where Δ is the wall thickness, and η is its resistivity.

The impact of distance of the conducting wall from the plasma on overall performance of the equilibrium also was examined. This was done at the aspect ratio 4.0. Note the reference case of the conducting wall at $0.3a$ results in the $n \to \infty$ ballooning and low-n kink stability limits to nearly coincide, while providing excellent bootstrap-current alignment. For wall positions of $0.25a$ or less the plasma stability was limited by ballooning modes, since the closer wall significantly raised the stability limit for low-n kink

modes. Therefore, moving the conducting wall closer than $0.3a$ does not result in any improvement in β. In principle, a more peaked pressure profile can be used to raise the ballooning stability limit and take advantage of the increased low-n kink stability limit. However, as discussed above, this will lead to poor bootstrap alignment.

These results indicate that for $A = 4$ and an elongation of 1.7 (triangularity of 0.5) at the 95% flux surface, the highest β_N possible, in conjunction with a bootstrap fraction that exceeds 90%, can be no larger than about 5.35, for a conducting wall closer than or equal to $0.25a$. At an elongation of 1.8 and triangularity of 0.5 the corresponding maximum $\beta_N = 5.6\%$.

7.2.1.2. Plasma shape

The plasma shape (elongation and triangularity) has a strong impact on the MHD stability. In particular, the plasma triangularity provides benefits for $n \to \infty$ ballooning modes by enhancing the good curvature along a magnetic field line, and for low-n external kink modes by enhancing the global magnetic shear at the plasma edge. This latter point is especially important for reversed-shear equilibria because moving the minimum in the safety factor closer to the plasma boundary tends to reduce magnetic shear there. Even though a conducting wall is used to aid in stabilizing low-n external kink modes, sufficient shear in the plasma still must be present to obtain full stabilization.

A scan of the maximum achievable β_N as a function of the plasma triangularity (ranging from 0.2 to 0.6) was performed. These calculations were done with a fixed elongation of 1.8, aspect ratio of 4.0, and safety factor at the plasma edge of approximately 3.5. This scan showed that β_N increases rapidly with increasing triangularity up to 0.4, and increases at a significant, but slower rate above this value. Since the edge safety factor was fixed during the scan, the plasma current increased (or q_* decreased) as the triangularity increased. Therefore, the β would increase faster than β_N because of $\beta \propto \beta_N/q_*$ scaling. These results are given in Table 7.2-II. The maximum triangularity is limited by the ability to design a divertor for the inboard separatrix that allows sufficient neutron shielding.

Increasing plasma elongation increases plasma β, both from increased plasma current and increased magnetic shear. However, elongation cannot be increased indefinitely as the plasma becomes more vertically unstable. Conducting structures and feedback control systems are required to stabilize this axisymmetric mode and they set the maximum practical value of plasma elongation.

Table 7.2-II.
Variation of Maximum β with Triangularity at A=4.0

Triangularity	Maximum β_N	Maximum β	q_*	Plasma Current (MA)
0.20	2.15%	2.00%	2.85	8.95
0.30	3.20%	3.13%	2.69	9.47
0.40	4.30%	4.60%	2.48	10.3
0.50	4.85%	5.45%	2.35	10.8
0.60	5.15%	6.25%	2.18	11.7

The conducting structure surrounding the plasma is designed to provide a safety factor, defined as $f_s = 1 + \tau_g/\tau_{L/R} = 1.2$ where τ_g and $\tau_{L/R}$ are the plasma vertical growth and the structure eddy current L/R time constants. This safety factor represents the margin to ideal instability where the plasma is uncontrollable (at $f_s = 1.0$). The distance of the conducting structure and its poloidal extent are determined to meet this criteria. Once this is established then the resistivity and thickness of the structure are chosen to allow for a reasonable feedback control power.

Vertical stability and dynamic control simulations were performed for the reversed-shear strawman designs listed in Table 7.3-I. The required structure on the outboard extends only from 55° to 90° at a distance of $0.5a$ measured radially outward from the plasma boundary. The inboard structure extends from 45° to 55° at $0.35a$. The locations of both of these structures are chosen so that they can be located behind the blanket and reflector. As such, the plasma elongation at the separatrix (and the 95% flux surface) had to be reduced from 2.0 to 1.9 (1.8 to 1.7). The structures are assumed to be made of 4-cm thick tungsten and electrically continuous in the toroidal direction.

The control requirement is to provide for a 1-cm RMS random disturbance with time scale equal to the plasma vertical growth time. The feedback control coils can be located in the middle of the outboard plates at $\sim 72°$, resulting in a peak power of 15 MVA. If the feedback control coils are located behind the shield, the peak power is 40 MVA. Note that this is mostly a reactive power and the required active power is substantially lower.

7.2.2. Current Drive

Although the reversed-shear configuration can have good bootstrap-current alignment, non-inductive techniques are required to drive current at the plasma center, and in some cases off axis. Two approaches were taken in estimating the required current-drive power. The first technique attempts to obtain an optimum match to the target equilibrium current-density profile with the sum of externally driven currents by RF waves and the bootstrap current. The second approach uses the sum of externally driven and bootstrap currents to self-consistently arrive at an equilibrium (different from the target) that is MHD stable yet maintains the relevant global features of the target equilibrium. The first method allows for quick estimates of the current-drive power requirement and is useful for parametric studies; however it is not totally self-consistent since the externally driven currents computed will not exactly match those assumed when computing the original equilibrium. The second is self-consistent in this sense, but it requires time-consuming computations for convergence to a final equilibrium (which is usually different from the starting equilibrium).

The first approach has been used in determining scalings of the bootstrap-aided current-drive efficiency, $\gamma_B \equiv \langle n_{e,20} \rangle I_p(A) R(m)/P_{CD}(W)$, with the volume-averaged electron temperature, $\langle T_e \rangle$, and aspect ratio, A. The four equilibria for $A = 3.0$, 3.5, 4.0 and 4.5 are given in Table 7.2-I. Three RF current-drive techniques have been examined for use with the reversed-shear configuration, namely, fast waves in the ion cyclotron range of frequencies (ICRF) for on-axis current drive, high-frequency (in the 15–20^{th} ion harmonic range) fast waves for off-axis current drive, and lower-hybrid waves for edge current drive. The calculations are done using the ray tracing code, CURRAY [12], that has been benchmarked with fast-wave current-drive experiments on DIII-D. An approximate match of the current profiles is obtained by selecting a combination of RF antenna-like power spectra and their launch locations.

The scalings of γ_B with the volume-averaged electron temperature and aspect ratio are displayed in Fig. 7.2-1. In Table 7.2-III, the power requirements for the three RF systems are displayed, each at an average electron temperature of $\langle T_e \rangle = 12$ keV. For completeness, the RF frequency and the launched parallel index of refraction, $N_{\|}$, for each current-drive system are also given. It is noted that for this series of calculations, the FWCD and HFFWCD techniques alone are sufficient to drive the seed currents on- and off-axis. The current-drive efficiency scalings shown in Fig. 7.2-1 and the wave parameters in Table 7.2-III have been used in the systems assessment given in Sec. 7.3.

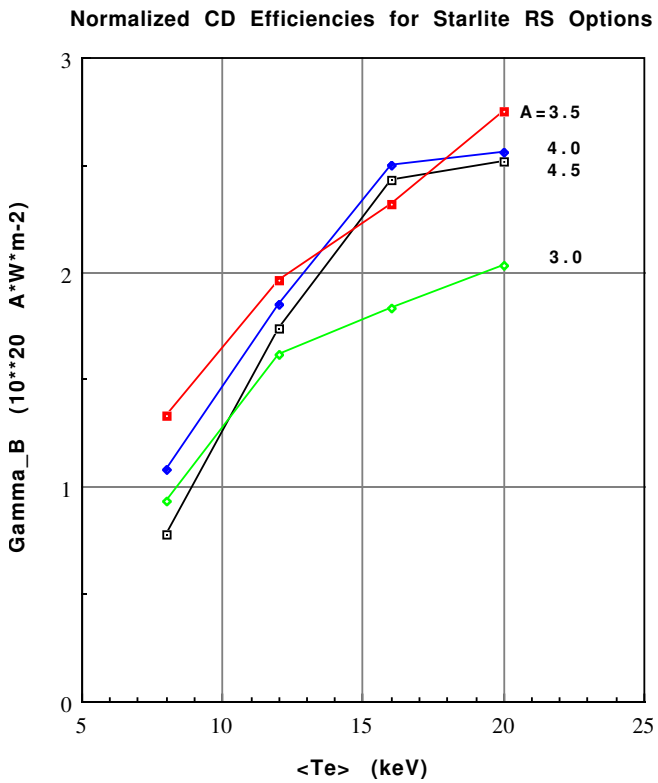

Figure 7.2-1. Normalized current-drive efficiency, γ_B, as a function of average electron temperature, $\langle T_e \rangle$, and aspect ratio, A, for the reversed-shear equilibria of Table 7.2-I.

The second approach to current-drive power assessment has been applied to a target reversed-shear equilibrium. Using the bootstrap model described in [13], and including a heuristic model to account for fast α particle effects, self-consistent bootstrap and current-drive calculations are done. The calculation iterates between the plasma equilibrium and the bootstrap/ray-tracing, providing the current-density profile consistent with the equilibrium [14]. An MHD stable equilibrium at $A = 4.5$ was taken as the target. An ICRF fast wave antenna power distribution was found that nearly duplicated the required seed current from the target. This equilibrium was subsequently tested for MHD stability, and was found to be stable.

The result of the FWCD calculation is shown in Fig. 7.2-2. The upper left plot shows the total, bootstrap, and FWCD parallel current-density profiles, given in the form of $\langle j \cdot B \rangle / \langle B^2 \rangle$. Also shown are the plasma density and temperature profiles, and the assumed plasma charge was $Z_{eff} = 1.34$ with $n_e/n_i = 1.16$. Note that the FWCD peaks near the magnetic axis, which is typical of fast wave damping at the location of

Table 7.2-III.
Current-Drive Power Requirements for the Reversed-Shear Equilibria[(a)]

	$A = 3.0$	$A = 3.5$	$A = 4.0$	$A = 4.5$
ICRF Fast Wave:				
current-drive Power (MW)	58.0	55.5	34.4	61.7
Frequency (MHz)	68	79	90	102
Launched $N_\parallel$	2.5	3.2	2.9	3.0
High-frequency Fast Wave:				
Current-drive Power (MW)	78.0	40.2	47.9	18.5
Frequency (GHz)	0.95	1.05	1.05	0.95
Launched $N_\parallel$	3.0	2.5	3.0	3.0
Total current-drive Power (MW)	136.	95.7	82.3	80.2
Current-drive Efficiency, γ_B	1.62	1.96	1.85	1.74

(*a*) For the equilibria of Table 7.2-I at $\langle T_e \rangle = 12$ keV.

the peak β. By careful adjustment of the FWCD launcher power, the result has the appropriate seed current to provide a stable reversed-shear q-profile, shown at the lower right. For this particular case, only current drive at the plasma axis was necessary, with bootstrap current providing the rest of the profile. Thus, only a single current drive frequency was required. In contrast to lower hybrid (LHCD) or high-frequency fast wave (HFFW) current drive, the present system has a high electrical efficiency and low unit cost. For the case examined ($B_T = 7.07$ T, $R = 5.99$ m) and the selected frequency of 78 MHz (with $n_\parallel = 2.4$), only the second tritium cyclotron harmonic is present in the plasma at $R = 5.3$ m. Only 12% of the power is lost to ion heating and 99% of the launcher power is absorbed in a single pass. The central electron and ion temperatures were 22 and 20 keV, respectively, with a peak electron density of 2.9×10^{20} m^{-3}.

This self-consistent approach also has been used to derive a temperature scaling of γ_B. For the case discussed above, the current-drive power was 59.2 MW, resulting in a γ_B

value of 1.73. In addition, at this frequency the electric-to-RF power conversion efficiency is 0.80. Several other cases were examined with different electron temperatures, although maintaining the same profile shape. In all cases the plasma remains nearly collisionless over the majority of the plasma, and the resulting current-drive efficiency is plotted in Fig. 7.2-3. An analytic fit to this dependence is $\gamma_B = 0.38\langle T\rangle^{0.56}$, where the brackets refer to volume average and the temperature is in keV. However, the current-drive efficiencies calculated using this self-consistent approach generally come out to be lower than those calculated from the first approach. We are presently trying to resolve this apparent discrepancy.

An initial survey of the current-drive requirements for the reversed-shear configuration points to the potential requirement of three RF techniques for current generation in various regions of the plasma. However, as indicated in the above examples, elimination of one or even two of the techniques at steady-state operation might be possible, leading to a simpler and potentially more economical current-drive system. The database for current drive using ICRF fast waves and lower hybrid waves has been well developed (see Sec. 5), whereas current drive by fast waves in the 15–20^{th} ion cyclotron harmonics has not yet been demonstrated. One should note, however, that most of the DIII-D fast wave current-drive experiments [15] have been carried out in the 4–10^{th} ion harmonic range. Driving currents off-axis in the bulk plasma region will remain an important issue for reversed-shear plasmas until an efficient technique is identified and demonstrated.

7.3. SYSTEMS ASSESSMENT

Systems analysis has been used to identify the cost optimum values of the plasma minor radius, a_p; the plasma aspect ratio, A; and the plasma ion temperature, T_i, for the reversed-shear design. The analysis presented herein will serve as the basis for selecting the design values of A and T_i. However, minor refinements in the radial build of the inboard blanket and/or shield are anticipated and should result in minor changes to a_p only.

The models used in the ARIES Systems Code (ASC) are described in Refs. [13] and [16]. Those models that have been developed specifically for the reversed-shear design (*i.e.*, scalings for normalized-β, β_N, and current-drive efficiency, γ_B) are discussed as needed in the text. All analysis is done for a 1-GWe power plant. The blanket and shield utilize vanadium alloys as the structural material and liquid lithium as the coolant and breeder. The blanket and shield used here are refinements of the ARIES-II blanket and shield designs and are described in Sec. 6.3 is used.

Figure 7.2-2. A self-consistent reversed-shear equilibrium with FWCD and bootstrap current at $A = 4.5$.

Figure 7.2-3. Bootstrap assisted γ_B for FWCD as a function of electron temperature for a reversed-shear case with $A = 4.5$, $Z_{av} = 1.16$, and $Z_{eff} = 1.34$.

7.3.1. Plasma Minor Radius

The most basic design parameter is the size of the tokamak. Typically, the ASC determines the plasma minor radius that minimizes the cost of electricity (COE) for a specified plasma aspect ratio and ion temperature. To limit the computational time associated with the PF-coil location algorithm, these parametric scans are restricted to a narrow range about the anticipated optimum minor radius. The COE for such a scan in a_p is shown in Fig. 7.3-1 for the reversed-shear design. As has been shown in the earlier ARIES-II/IV designs [13], if unconstrained, the COE will display a minimum in minor radius resulting from the maximization of the Fusion Power Core (FPC) mass power density (MPD) that is driven primarily by TF-coil mass. However, three constraints can restrict the minimum plasma minor radius allowed: (1) The peak field at the TF coil is constrained to $B_{TF} \leq 16$ T [13]; (2) The peak neutron wall loading is constrained to $\hat{I}_w \leq 10.4$ MW/m^2 for a vanadium first wall [13]; and (3) No structures comprising the inboard radial build may overlap. The peak-field constraint is more restrictive than the wall-loading constraint for reversed-shear designs and is the limiting constraint for $A \geq 3.5$. At $A = 3$ the minimum minor radius is limited by the inboard radial build.

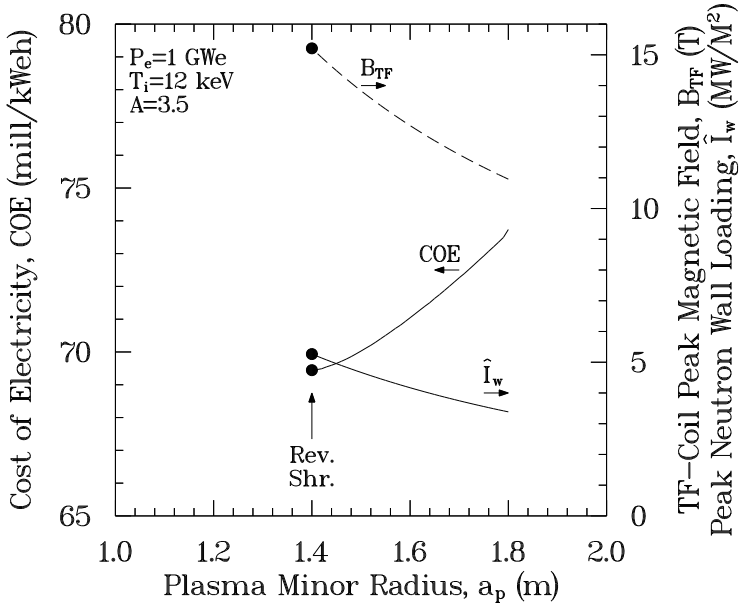

Figure 7.3-1. Cost of electricity as a function of plasma minor radius calculated internally to the ASC for the given reversed-shear parameters.

7.3.2. Plasma Ion Temperature

The cost-of-electricity sensitivity to variations in the plasma ion temperature is shown in Fig. 7.3-2. The COE is strongly dependent upon temperature below 10 keV, but only weakly dependent upon temperature between 10 and 20 keV. The temperature that minimizes the COE also maximizes the mass power density, as is shown in Fig. 7.3-3. The engineering gain (defined as the ratio of the gross electric to recirculating powers) is usually an equally important contributor to COE; but is influential only at low temperature for reversed shear even though the engineering gain and its underlying driver, current-drive efficiency, monotonicly increase with increasing temperature over the entire temperature range examined (see Fig. 7.3-3). At the lowest temperatures the increasing engineering gain with increasing temperature decreases the COE and increases the MPD. At the COE minimum in temperature, the current-drive power becomes comparable to the rf capacity required to initially heat the plasma to ignition, and is no longer a major driver of COE. The MPD decreases with increasing temperature above the optimum

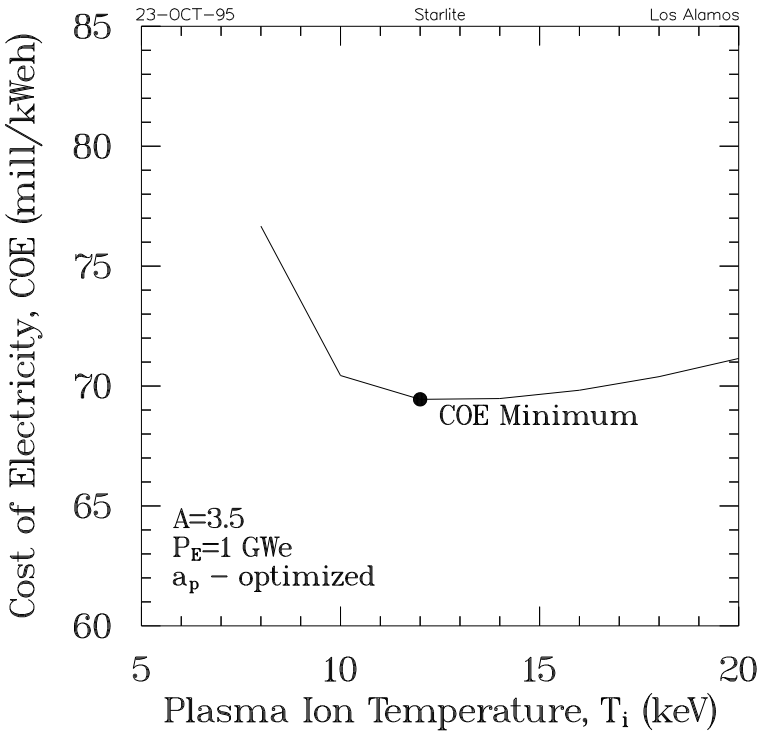

Figure 7.3-2. Cost of electricity for reversed shear parameters as a function of the plasma ion temperature. Each point along the curve represents the COE optimum in plasma minor radius, a_p.

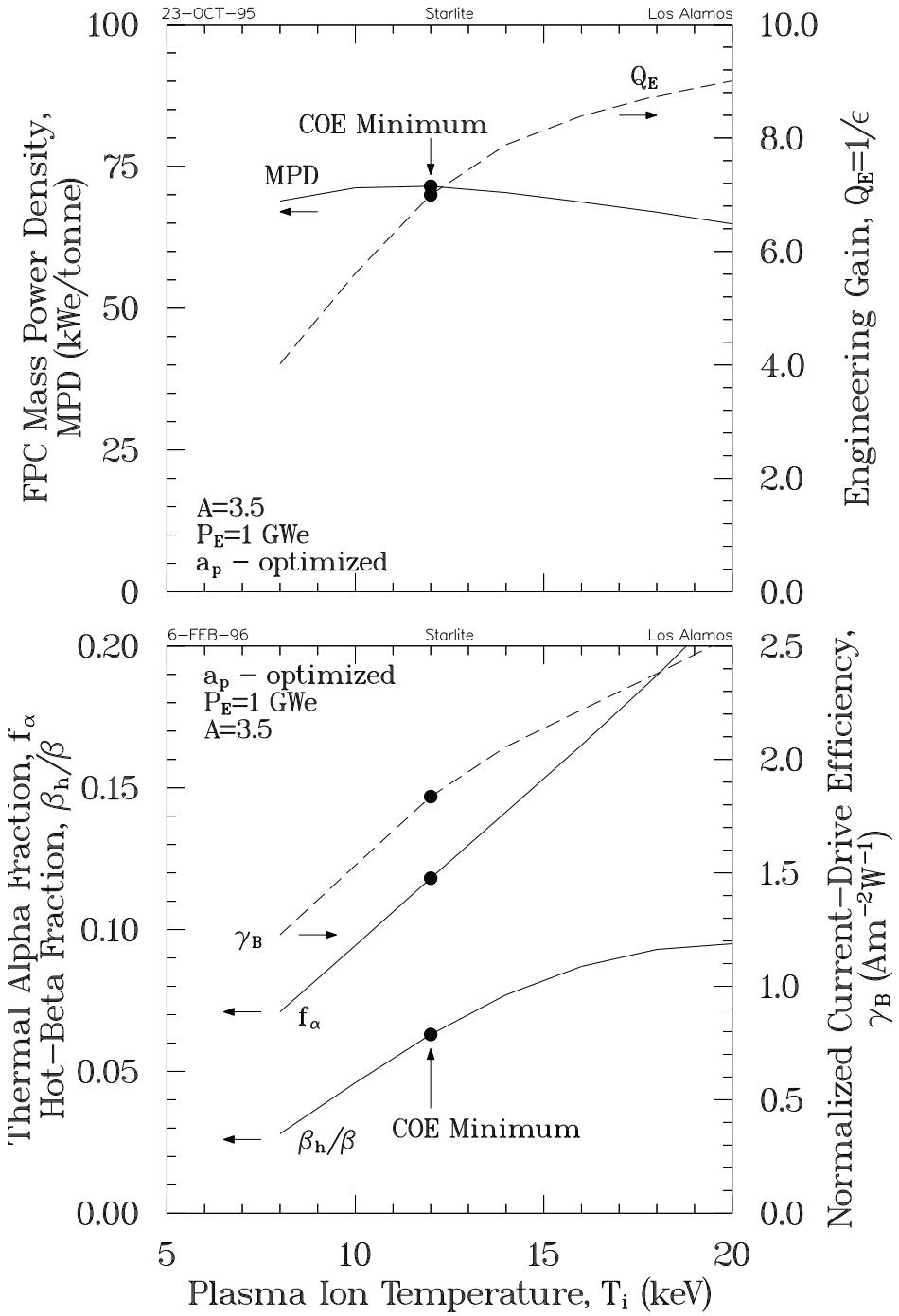

Figure 7.3-3. In the top frame are the mass power density and engineering gain, and in the bottom frame are the plasma thermal-α density fraction, hot β fraction, and current-drive efficiency for the ion-temperature variation of Fig. 7.3-2.

temperature because of decreased reactivity. In higher temperature, lower density plasmas (at constant β), fusion products are thermalized slower, increase the hot α-particle pressure (see Fig. 7.3-3), decrease the fuel pressure, and require increased toroidal field that increases TF-coil costs for the same net electrical power. The optimum temperature varies slightly (from 12 to 14 keV) with aspect ratio because of the dependencies of γ_B with A and T_i, as is discussed in Sec. 7.3.3.

7.3.3. Plasma Aspect Ratio

The dependency of the COE upon plasma aspect ratio is shown in Fig. 7.3-4 for reversed shear parameters. The COE minimum in plasma aspect ratio occurs at $A = 3.5$. As was the case for the COE minimum in temperature, the aspect ratio that minimizes the COE also maximizes the mass power density (MPD), as is shown in Fig. 7.3-5. Because

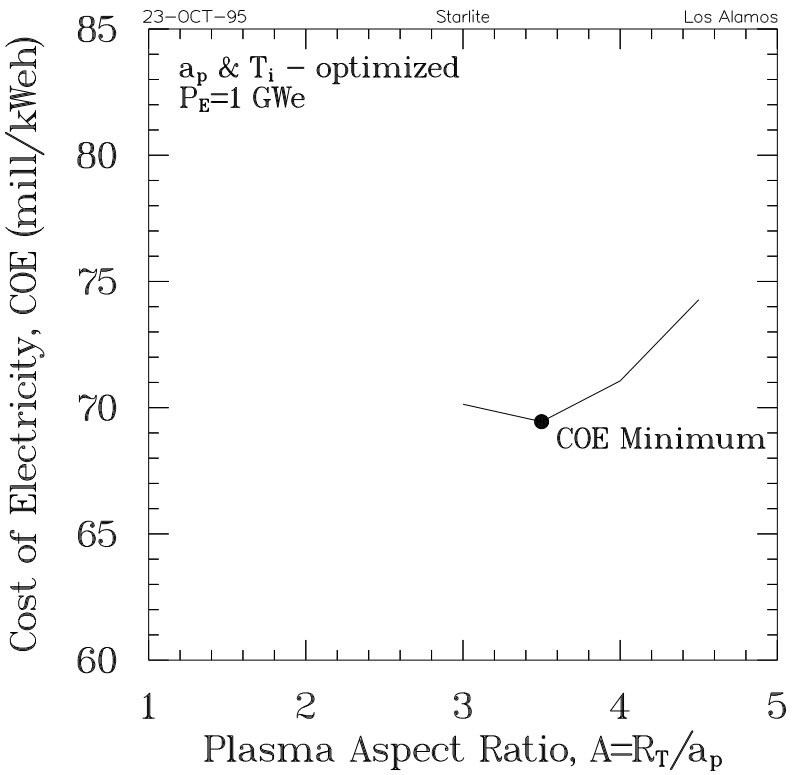

Figure 7.3-4. The cost of electricity for reversed shear parameters as a function of the plasma aspect ratio. Each point along the curve represents the COE optimum in plasma minor radius, a_p, and ion temperature, T_i.

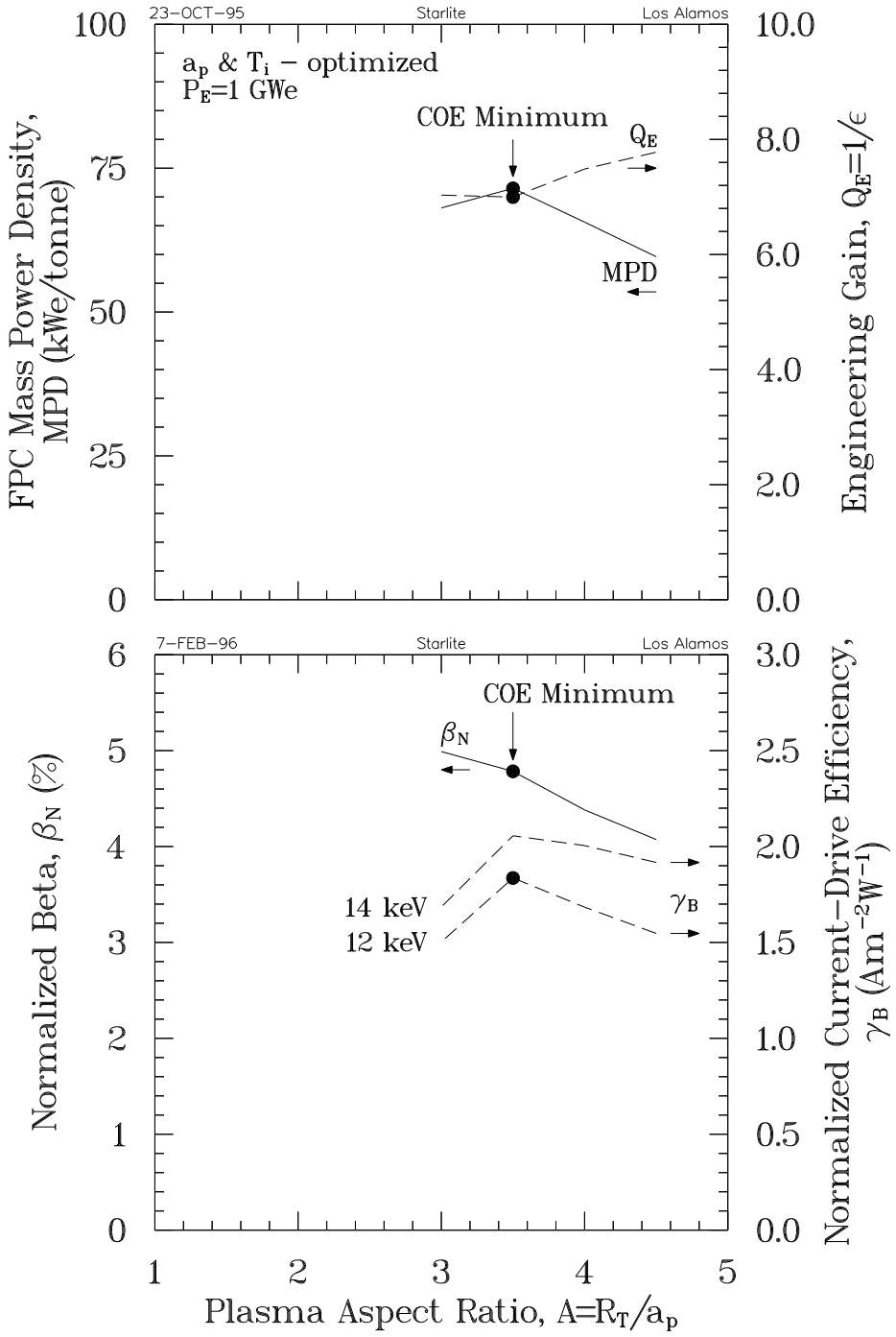

Figure 7.3-5. In the top frame are the mass power density (left scale) and engineering gain (right scale), and in the bottom frame are the plasma normalized β (left scale) and the plasma current-drive efficiency (right scale) for the aspect-ratio variation of Fig. 7.3-4.

the engineering gain is relatively high, MPD is the primary discriminating factor in determining the COE minimum in aspect ratio. The aspect ratio that maximizes the MPD maximizes fusion power density (*i.e.*, $\beta^2 B_{\phi 0}^4$) and is determined by the β_N scaling, which increases monotonicly with decreasing aspect ratio and is shown in Fig. 7.3-5, and by the reduction in on-axis toroidal field that occurs with decreasing aspect ratio, as is shown in Fig. 7.3-6.

That the engineering gain is a minimum at the aspect ratio corresponding to the COE minimum is coincidental. The engineering-gain dependency upon aspect ratio is contrary to the current-drive efficiency dependency upon aspect ratio. The counterbalancing factor is the wall-plug current-drive efficiency, which changes with both aspect ratio and temperature to produce the engineering-gain dependency upon aspect ratio shown in Fig. 7.3-5, because the current-drive frequencies are functions of aspect ratio and temperature.

The optimum plasma temperature as a function of aspect ratio is shown Fig. 7.3-6. The optimum temperature is lowered at $A = 3.5$ to take advantage of a reduction in hot α pressure (Fig. 7.3-6) and accompanying increase in the fuel pressure in spite of the disadvantage associated with a reduction in current-drive efficiency (Fig. 7.3-5).

7.3.4. Design Point Determination

Having determined the cost-based optimum plasma aspect ratio and ion temperature, a nearby point was chosen for development of a detailed power-plant design. Observing that the COE variation within the range $3 \leq A \leq 4$ is not significant, engineering-design issues related to aspect ratio that are described in Sec. 6 pushed the reference design to $A = 4$. Minor modifications to the inboard radial build have occurred since the parametric analysis of Sec. 7.3.1 through 7.3.3 that have added approximately 1 mill/kWeh to the COE. These engineering changes have been counterbalanced by a physics change (see Sec. 5) that moves the kink stabilizing shell from $b/a = 1.30$ to $b/a = 1.25$ and results in an increases in β from 4.9% to 5.3% and a reduction in the COE by approximately 1 mill/kWeh. A list of parameter for the present reference design are given in Tables 7.3-I through 7.3-III.

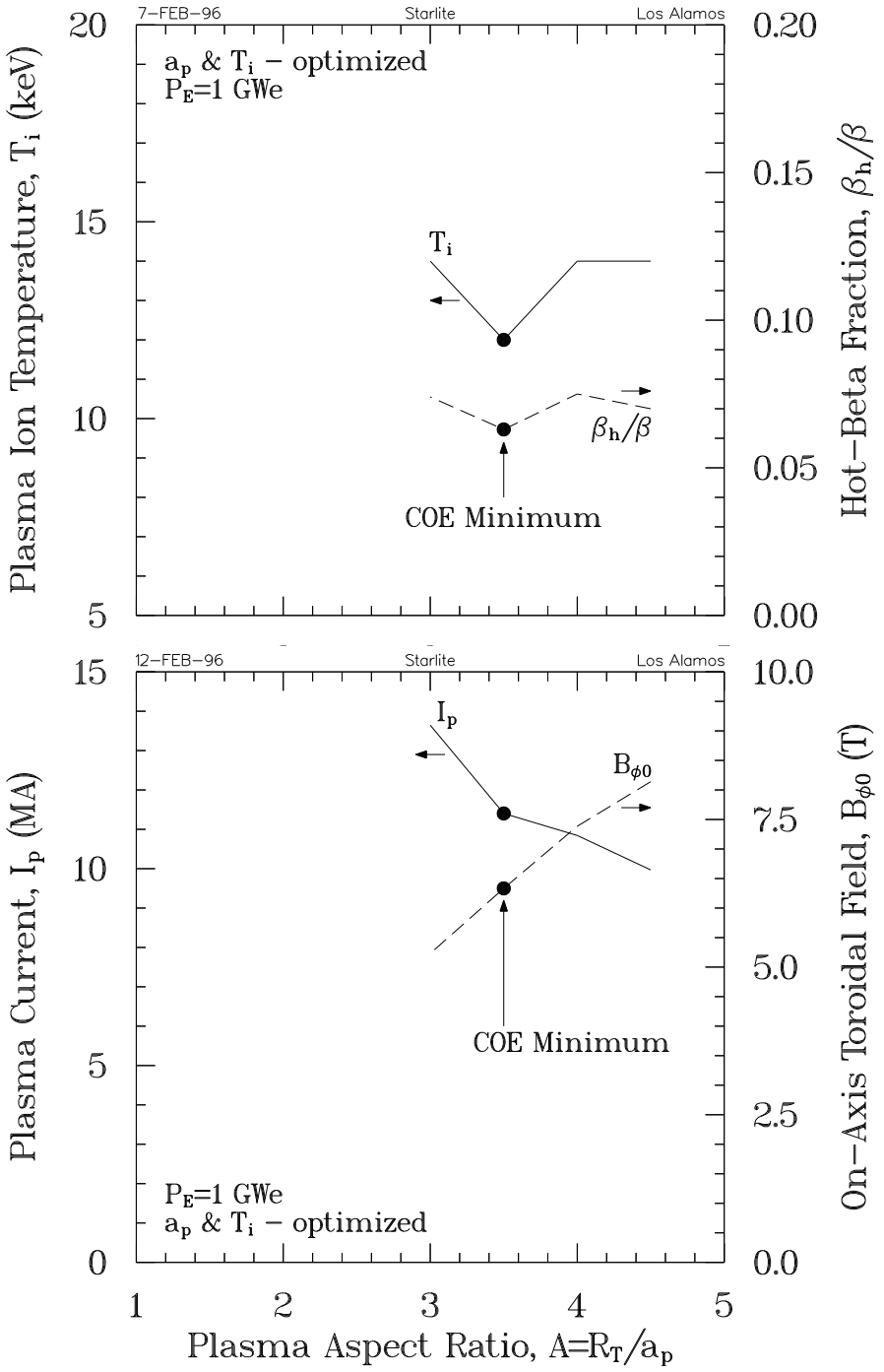

Figure 7.3-6. In the top frame are the plasma ion temperature (left scale) and the hot β fraction (right scale), and in the bottom frame are the plasma current (left scale) and the on-axis toroidal field (right scale) for the aspect-ratio variation of Fig. 7.3-4.

Table 7.3-I.
Reversed-Shear Power-Plant Physics Parameters

Plasma major toroidal radius, R_T (m)	5.04
Plasma minor radius, a_p (m)	1.26
Plasma vertical elongation, $\kappa_\times$	2.00
Plasma vertical elongation, κ_{95}	1.80
Plasma triangularity, $\delta_\times$	0.68
Plasma triangularity, δ_{95}	0.50
Plasma aspect ratio, $A = R_T/a_p$	4.00
On-axis safety factor, q_0	2.82
Circularized safety factor, q_*	2.37
Plasma-edge safety factor, q	3.51
Troyon coefficient, C_T (Tm/MA)	4.76
Plasma β	5.31
Plasma poloidal β	2.26
Stability parameter, $\epsilon\beta_p$	0.56
Peak-to-average density, n_0/n	1.42
Peak-to-average temperature, T_0/T	1.46
Normalized edge density, n_E/n	0.29
Ion temperature, T_i (keV)	14.0
Electron temperature, T_e (keV)	14.7
Ion density, n_i (10^{20} m^{-3})	2.07
Electron density, n_e (10^{20} m^{-3})	2.50
Particle-to-energy confinement time ratio, τ_p/τ_E	4.00
Ion-to-electron energy confinement time ratio, τ_{Ei}/τ_{Ee}	1.00
Lawson parameter, $n_i\tau_E$ (10^{20} m^{-3}s)	2.58
ITER-89P scaling [17] multiplier, H_{89P}	2.40
On-axis toroidal field, $B_{\phi 0}$ (T)	7.35
Radiation fraction, f_{RAD}	0.19
Plasma current, I_p (MA)	10.3
Bootstrap-current fraction, f_{BC}	0.89
Current-drive power to plasma, P_{CD} (MW)	64.7
Current-drive efficiencies:	
I_{EX}/P_{CD} (mA/W)	159.8
γ (10^{20} A/W-m^2)	2.02

Table 7.3-II.
Reversed-Shear Power-Plant Engineering Parameters

Field at TF coil, B_{TF} (T)	15.7
TF-coil stress (MPa)	511.8
TF-coil current density, j_{TF} (MA/m^2)	34.5
Magnetic-field energy, W_B (GJ)	81.9
Total specific energy, W_B/M_c (MJ/tonne)	27.5
Fusion power, P_F (GW)	1.88
Neutron power, P_N (GW)	1.50
Average neutron wall loading, I_w (MW/m^2)	3.96
Peak neutron wall loading, $\hat{I}_w$ (MW/m^2)	5.74
Neutron fluence life, $I_w\tau$ (MWy/m^2)	12.0
Average blanket energy multiplication	1.37
Average first-wall heat flux, q_w (MW/m^2)	0.43
Blanket power density, P_{TH}/V_{BLK} (MW/m^3)	12.86
Current-drive system efficiency, η_{CD}	0.69
Thermal conversion efficiency, η_{TH}	0.46
Thermal power (GWth):	
peak, $\hat{P}_{TH}$	2.50
average, P_{TH}	2.50
Auxiliary site power, P_{AUX} (MW)	46.1
Primary loop pumping power (MW)	11.5
Gross electrical power, P_{ET} (GWe)	1.15
Net electrical power, P_E (GWe)	1.00
Recirculating-power fraction, $\epsilon = 1/Q_E$	0.13
Plasma gain, $Q_p = P_F/P_{CD}$	29.0
Engineering gain, Q_E	7.61
Net plant efficiency, $\eta_p = \eta_{TH}(1-\epsilon)$	0.40
Plant capacity factor, p_f	0.76
Masses (tonne):	
First wall	5.6
Blanket and reflector	384
Shield	3,540
TF coils	1,277
PF coils	1,701
Fusion power core	9,878
Mass power density, MPD (kWe/tonne)	70.8
Level of Safety Assurance, LSA	2

Table 7.3-III.
Reversed-Shear Power-Plant Economic Parameters (1992 $)

Acct. No.	Account Title	Million Dollars
20.	Land and land rights	10.4
21.	Structures and site facilities	324.8
22.	Reactor plant equipment	1,172.4
22.1.1	First wall, Blanket, and Reflector	47.0
22.1.2	Shield	166.7
22.1.3	Magnets	244.5
	TF coils	112.5
	PF coils	132.1
22.1.4	Supplemental heating systems	162.0
22.1.5	Primary structure and support	39.0
22.1.6	Reactor vacuum systems	68.5
22.1.7	Power supplies	55.3
22.1.8	Impurity control	3.9
22.1.9	Direct energy conversion system	0.0
22.1.10	ECRH breakdown system	4.3
22.1	Reactor equipment	791.0
22.2	Main Heat Transfer and Transport	228.5
23.	Turbine plant equipment	273.7
24.	Electric plant equipment	108.1
25.	Miscellaneous plant equipment	54.7
26.	Special materials	10.5
90.	Total direct cost	1,954.7
91.	Construction services and equipment	234.6
92.	Home office engineering and services	101.6
93.	Field office engineering and services	117.3
94.	Owner's costs	361.2
96.	Project contingency	467.4
97.	Interest during construction (IDC)	534.7
98.	Escalation during construction (EDC)	
99.	Total capital cost	3,771.4
		Constant dollars
[90]	Unit direct cost, UDC ($/kWe)	1,954.7
[94]	Unit base cost, UBC ($/kWe)	3,236.7
[99]	Unit total cost, UTC ($/kWe)	3,771.4
	Capital return (mill/kWeh)	54.76
[40-47,51]	O&M (1.4%) (mill/kWeh)	9.16
[50]	Blanket replacement (mill/kWeh)	5.27
	Decommissioning (mill/kWeh)	0.50
[02]	Fuel (mill/kWeh)	0.03
	Cost of electricity, COE (mill/kWeh)	69.72

7.4. SUMMARY AND CONCLUSIONS

The reversed-shear plasma configuration achieves both high β_N and high β, it obtains large bootstrap current fractions with very good current profile alignment, and it appears to provide the transport suppression necessary to sustain the pressure profile that is consistent with the higher β and high bootstrap current. Recent experiments have demonstrated transiently the improved MHD stability and suppression of plasma particle and energy transport. Complete demonstration of all the favorable properties simultaneously will require steady-state conditions, which are not accessible in present experimental devices.

Several reversed-shear equilibria were examined in order to assess the balance between maximizing β (fusion power density) and minimizing the current-drive (recirculating) power. The impact of plasma shape, elongation, aspect ratio, and location of conducting shell for the stabilization of low-n kink modes were investigated. An initial survey of the current-drive requirements for the reversed-shear configuration points to the potential requirement of three RF techniques for current generation at three locations: on-axis (ICRF fast-wave), mid-plasma (high-frequency fast-wave), and edge-plasma (lower hybrid). The database for current drive using ICRF fast waves and lower hybrid waves have been well developed, whereas current drive by fast waves in the 15–20^{th} ion cyclotron harmonics has not yet been demonstrated. Other aternatives such as mode-conversion and electron-cyclotron current-drive also can be used in the mid-plasma region. Driving currents off-axis in the bulk plasma region will remain an important issue for reversed-shear plasmas until an efficient technique is identified and demonstrated.

The assessment of engineering options of Sec. 6 applies to this regime of operation (noting that reversed-shear plasmas probably lead to devices with higher neutron and surface heat loads). Systems analysis has been used to identify the cost optimum values of the plasma minor radius, a_p; the plasma aspect ratio, A; and the plasma ion temperature, T_i, for the reversed-shear design. It was found that COE variation within the range $3 \leq A \leq 4$ is not significant. Engineering-design issues related to aspect ratio that are described in Sec. 6 pushed the reference design to $A = 4$. Overall the reversed-shear plasma offers the best economic performance of physics options examined and the data base for this regime, while small, is growing rapidly.

REFERENCES

[1] C. E. Kessel, J. Manickam, G. Rewoldt, *et al.*, "Improved Plasma Performance in Tokamaks with Negative Magnetic Shear," *Phys. Rev. Let.,* **72** (1994) 1212.

[2] T. Ozeki *et al.*, "Profile Control for Stable High-β_p Tokamaks with Large Bootstrap Current," *Proc. 14th Int. Conf. on Plasma Phys. and Controlled Nucl. Fusion Research,* Würzburg, Germany (Oct. 1992), International Atomic Energy Agency, Vienna (1993).

[3] A. D. Turnbull, T. S. Taylor, Y. R. Lin-Liu, *et al.*, "High Beta and Enhanced Confinement in a Second Stable Core VH-Mode Advanced Tokamak," *Phys. Rev. Let.,* **74** (1995) 718.

[4] F. Levinton, M. C. Zarnstorff, S. H. Batha, *et al.*, "Improved Confinement with Reversed Magnetic Shear in TFTR," *Phys. Rev. Let.,* **75** (1995) 4417.

[5] E. J. Strait, L. L. Lao, M. E. Mauel, *et al.*, "Enhanced Confinement and Stability in DIII-D Discharges with Reversed Magnetic Shear," *Phys. Rev. Letters,* **75** (1995) 4420.

[6] L. L. Lao, K. H. Burrell, T. S. Casper, *et al.*, "Confinement and Stability of DIII-D Negative Central Shear Discharges," *Plasma Phys. Control. Fusion,* **38** (1996) 1439.

[7] C. E. Kessel, "The Bootstrap Current in a Tokamak," *Nucl. Fusion,* **34** (1994) 1221.

[8] J. M. Greene and M. S. Chance, "The Second Region of Stability Against Ballooning Modes," *Nucl. Fusion,* **21** (1981) 453.

[9] M. J. Gerver, J. Kesner, and J. J. Ramos, "Access to the Second Stability Region in a High-Shear, Low- Aspect-Ratio Tokamak," *Phys. Fluids,* **31** (1988) 2674.

[10] T. S. Taylor, E. J. Strait, L. L. Lao, *et al.*, "Wall Stabilization of High Beta Plasmas in DIII-D," *Phys. Plasmas,* **2** (1995) 2390.

[11] A. Bondeson and D. J. Ward, "Stabilization of External Modes in Tokamaks by Resistive Walls and Plasma Rotation," *Phys. Rev. Lett.,* **72** (1994) 2709.

[12] T. K. Mau, S. C. Chiu, R. W. Harvey, "Modelling of Fast Wave Current Drive in Standard and Second-Stability Bootstrapped Reactor Plasmas," *Proc. EPS Top. Conf. on Radiofrequency Heating and Current Drive of Fusion Devices,* Brussels (1992) 173.

[13] F. Najmabadi, R. W. Conn, *et al.*, "The ARIES-II and -IV Second-Stability Tokamak Fusion Power Plant Study—The Final Report," UCLA report UCLA-PPG-1461 (to be published); also, F. Najmabadi, R. W. Conn, *et al.*, "Directions for Attractive Tokamak Reactors: The ARIES-II and ARIES-IV Second-Stability Designs," *Proc. 14th Int. Conf. on Plasma Phys. and Controlled Nucl. Fusion Research,* Würzburg, Germany (Oct. 1992), International Atomic Energy Agency, Vienna (1993) 295.

[14] D. A. Ehst and C. F. F. Karney, "Approximate Formula for Radio-Frequency Current Drive Efficiency with Magnetic Trapping," *Nucl. Fusion* **31** (1991) 1933.

[15] J. S. deGrassie, C. C. Petty, R. I. Pinsker, *et al.,* "Fast Wave Current Drive on DIII-D," *Proc. 11th Top. Conf. on Radio Frequency Power in Plasmas,* Palm Springs, CA (1995) 173.

[16] F. Najmabadi *et al.*, "The Pulsar Study– A Pulsed-Tokamak Fusion Power Plant," University of California, San Diego report UCSD-ENG-003 (1996).

[17] D. E. Post, K. Borrass, J. D. Callen, S. A. Cohen, J. G. Cordey, F. Engelmann, *et al.*, "ITER Physics," International Thermonuclear Experimental Reactor documentation series No. 21 (November 1990).